

Asymmetric fission of ^{180}Hg and the role of hexadecapole moment*

Yang Su,¹ Yong-Jing Chen,¹ Ze-Yu Li,¹ Li-Le Liu,¹ Guo-xiang Dong,² and Xiao-bao Wang^{2,†}

¹China Nuclear Data Center, China Institute of Atomic Energy, Beijing 102413, China

²School of Science, Huzhou University, Huzhou 313000, China

In current work, the fission property of ^{180}Hg is investigated based on the Skyrme density functional theory (DFT). The impact of the high-order hexadecapole moment (q_{40}) is found at large deformations. With the q_{40} constraint, a smooth and continuous potential energy surfaces (PES) could be obtained. Especially, the hexadecapole moment constraint is essential to get proper scission configurations. The static fission path based on the PES supports the asymmetric fission of ^{180}Hg . The asymmetric distribution of the fission yields of ^{180}Hg is further reproduced by the time-dependent generator coordinate method (TDGCM), and agrees well with the experimental data.

Keywords: Nuclear fission, density functional theory, hexadecapole moment, potential energy surface, mass distribution

I. INTRODUCTION

The asymmetric fission mode in neutron-deficient ^{180}Hg has been discovered in 2010 via the β decay of ^{180}Tl [1]. For the fission of ^{180}Hg , its splitting into two ^{90}Zr fragments with magic $N = 50$ and semimagic $Z = 40$ was believed to dominate the fission process. However, unlike the initially theoretical prediction, ^{180}Hg has been observed to fission asymmetrically, with heavy and light fragment mass distribution centered around $A = 100$ and 80 nucleons, respectively [1, 2].

A lot of theoretical research attentions have been drawn to the puzzling fission behavior of ^{180}Hg . For example, the macroscopic-microscopic models [1, 3–5] and self-consistent microscopic approaches [6–8] were used to analyzing the multidimensional potential energy surfaces (PESs), and the presence of an asymmetric saddle point with a rather high ridge between symmetric and asymmetric fission valleys was explained as the main factor determining the mass split in fission.

The calculations of fission-fragment yields have also been done for ^{180}Hg by means of the Brownian Metropolis shape-motion treatment [3, 5, 9], Langevin equation [10], scission-point model [4, 11, 12], the random neck rupture mechanism [13], based on the PESs or scission configurations. The results are in approximate agreement with the experimental data, a deviation of ~ 4 nucleons for the peak positions. There were also several attempts to describe fragment mass distribution in a fully microscopic way, i.e., the time-dependent generator coordinate method (TDGCM) based on covariant density functional theory (CDFT) [8], and the asymmetric peaks are reproduced very well, while a more asymmetric fission mode with $A_H \sim 116$ is predicted, which was not observed in experimental measurement.

In the theoretical study of nuclear fission, the PES is an important infrastructure, which describe the evolution of nuclear

energies with its shape variations on its way from the initial configuration towards scission. In nuclear physics, there are generally two approaches to generate PES. One is ranging from the historical liquid drop model [14, 15] to the well-known macroscopic-microscopic model, using parametrization of the nuclear mean-field deformation [16–19]. The other is based on microscopic self-consistent methods [20–26], or the constrained relativistic mean-field method [8, 27–30].

In macroscopic-microscopic method, a predefined class of nuclear shapes were defined uniquely in terms of selecting appropriate collective coordinates, and the relatively smooth potential energy surface can be obtained. However, due to limitations in computing resources, the microscopic calculation of PES can only be performed within a limited number of deformation degrees of freedom. In microscopic self-consistent method, the higher-order collective degrees of freedom was incorporated self-consistently based on the variational principle. In fission studies, the quadrupole and octupole deformation (moments) constraints are the natural and most often used to calculate microscopic PES.

However, several studies have shown that as a consequence of the absence of hexadecapole deformation (q_{40} or β_4), PES may exhibit discontinuities in the large deformations scission regions [31–35]. Ref. [36] investigated the role of hexadecapole deformation on the PES calculation of ^{240}Pu by applying a disturbance on β_4 . The results show that one can obtain a smooth 2-dimensional PES in (β_2, β_3) by parallel calculations with a suitable disturbance of hexadecapole deformation.

But for asymmetric fission of ^{180}Hg , there have been no reports about the effect of q_{40} or β_4 on the PES of ^{180}Hg . The self-consistent calculation in quadrupole and octupole deformation spaces indicated that the PES of ^{180}Hg exhibits different behavior from that of ^{240}Pu or ^{236}U with increasing of the quadrupole moment [6, 8]. Thus it is interesting to examine the influence of hexadecapole moment on PES of ^{180}Hg at large deformation, and also analysis some properties of scission configuration. In this paper, we will extend two-dimensional (q_{20}, q_{30}) constraint calculations at large deformation region by adding q_{40} constraint on the microscopic PES calculation of ^{180}Hg . The importance of q_{40} in the self-consistent calculation of PES for ^{180}Hg at large deformation will be investigated. Moreover, the fission dynamic of

* This work has been supported by National Natural Science Foundation of China under Grant Nos. 12275081, U1732138, National Key R & D Program of China (No.2022YFA1602000) and Continuous-support Basic Scientific Research Project.

† Corresponding author, xbwang@zjhu.edu.cn

¹⁸⁰Hg, the total kinetic energies and the fragment mass yield distributions based on the TDGCM [37] will be described and discussed.

II. THEORETICAL FRAMEWORK

To study the static fission properties, the PES was determined by using the Skyrme density functional theory (DFT). The dynamic process is further investigated in the framework of TDGCM. Thus, in this section, we explain these two methods briefly. The detailed description of Skyrme DFT can be found in Ref. [38], and the formulations of TDGCM can be found in Refs. [37, 39–41].

A. Density functional theory

In the local density approximation of DFT, the total energy of finite nuclei can be calculated from the spatial integration of the Hamiltonian density $\mathcal{H}(\mathbf{r})$,

$$\mathcal{H}(\mathbf{r}) = \frac{\hbar^2}{2m} \tau(\mathbf{r}) + \sum_{t=0,1} \chi_t(\mathbf{r}) + \sum_{t=0,1} \check{\chi}_t(\mathbf{r}). \quad (1)$$

In the above equation, $\tau(\mathbf{r})$, $\chi_t(\mathbf{r})$ and $\check{\chi}_t(\mathbf{r})$ stand for the density of the kinetic energy, the potential energy and the pairing energy respectively. The symbol $t = 0, 1$ denotes the isoscalar or isovector, respectively [42].

The mean-field potential energy $\chi_t(\mathbf{r})$ in the Skyrme DFT has the form generally as

$$\chi_t(\mathbf{r}) = C_t^{\rho\rho} \rho_t^2 + C_t^{\rho\tau} \rho_t \tau_t + C_t^{J^2} \mathbb{J}_t^2 + C_t^{\rho\Delta\rho} \rho_t \Delta\rho_t + C_t^{\rho\nabla J} \rho_t \nabla \cdot \mathbf{J}_t \quad (2)$$

where the particle density ρ_t , kinetic density τ_t , and the spin current vector densities \mathbf{J}_t ($t = 0, 1$) can be calculated by the density matrix $\rho_t(\mathbf{r}\sigma, \mathbf{r}'\sigma')$, with the dependence of spatial (\mathbf{r}) and spin (σ) coordinates. And, $C_t^{\rho\rho}$, $C_t^{\rho\tau}$, and *etc.* are coupling constants for different types of densities in the Hamiltonian density $\mathcal{H}(\mathbf{r})$, which are usually real numbers. As an exception, $C_t^{\rho\rho} = C_{t0}^{\rho\rho} + C_{tD}^{\rho\rho} \rho_0^\gamma$ is the density-dependence term. The formulations of the relation of the coupling constants to traditional Skyrme parameters can be found in Ref. [43]. For example, spin-orbit force of the Skyrme interaction corresponds to the term $C_t^{\rho\nabla J} \rho_t \nabla \cdot \mathbf{J}_t$.

The pairing correlation is often taken into account through the Hartree-Fock-Bogoliubov (HFB) approximation in DFT [38]. In the case of the Skyrme energy density functional, a commonly adopted pairing force is the density-dependent surface-volume, zero-range potential, as given in Refs. [26, 44]:

$$\hat{V}_{\text{pair}}(\mathbf{r}, \mathbf{r}') = V_0^{(n,p)} \left[1 - \frac{1}{2} \frac{\rho(\mathbf{r})}{\rho_0} \right] \delta(\mathbf{r} - \mathbf{r}'), \quad (3)$$

where $V_0^{(n,p)}$ is the pairing strength for the neutron (n) and the proton (p), ρ_0 is the saturation density of nuclear matter fixed

as 0.16 fm^{-3} , and $\rho(\mathbf{r})$ indicates the total density. As studied in Ref. [26], this type of pairing force is a suitable choice for nuclear fission study.

The DFT solvers HFBTHO(V3.00) [45] is used to generate the PESs, in which the axial symmetry is assumed. 26 major shells of the axial harmonic-oscillator single-particle basis are used, and the number of the basis states are further truncated to be 1140. In this work, the Skyrme DFT with SkM* parameters [46] is adopted, which is commonly used for the fission study. For the strength of pairing, $v_0^{(n)} = -268.9 \text{ MeV fm}^3$ and $v_0^{(p)} = -332.5 \text{ MeV fm}^3$ are used for the neutron and the proton respectively, with the pairing window of $E_{\text{cut}} = 60 \text{ MeV}$. This pairing strength together with the choice of SkM* force and model space has been adopted in Refs. [6, 47], in which the two-dimensional PES related to the fission of ¹⁸⁰Hg has been studied.

B. Time-dependent generator coordinate method

The nuclear fission is a large-amplitude collective motion, which could be approximated as a slow adiabatic process driven by several collective degrees of freedom. In TDGCM, the many-body wave function of the fissioning system takes the generic form

$$|\Psi(t)\rangle = \int_{\mathbf{q}} f(\mathbf{q}, t) |\Phi(\mathbf{q})\rangle d\mathbf{q}. \quad (4)$$

where $|\Phi(\mathbf{q})\rangle$ is composed of known many-body wave functions with the vector of continuous variables \mathbf{q} . The \mathbf{q} are collections of variables chosen according to the physics problem.

For the fission study, two collective variables, quadrupole moment \hat{q}_{20} and octupole moment \hat{q}_{30} , are usually adopted. In the above equation, the $f(\mathbf{q}, t)$ is a weighted function. It is determined by the time-dependent Schrödinger-like equation, as

$$i\hbar \frac{\partial g(\mathbf{q}, t)}{\partial t} = \hat{H}_{\text{coll}}(\mathbf{q}) g(\mathbf{q}, t), \quad (5)$$

in which the Gaussian overlap approximation (GOA) is used. $\hat{H}_{\text{coll}}(\mathbf{q})$ is the collective Hamiltonian, as

$$\hat{H}_{\text{coll}}(\mathbf{q}) = -\frac{\hbar^2}{2} \sum_{ij} \frac{\partial}{\partial q_i} B_{ij}(\mathbf{q}) \frac{\partial}{\partial q_j} + V(\mathbf{q}), \quad (6)$$

in which $V(\mathbf{q})$ is the collective potential, and $B_{ij}(\mathbf{q}) = \mathcal{M}^{-1}(\mathbf{q})$ is the inertia tensor as the inverse of the mass tensor \mathcal{M} . The potential and mass tensor are solved by the Skyrme DFT in this work. $g(\mathbf{q}, t)$ contains the information about the dynamic of the fissioning nuclei, and is the complex collective wave function with collective variables \mathbf{q} .

To describe the nuclear fission, the collective space has been divided into an inner region and an external region respectively, for the nucleus staying as a whole and the nucleus separated into two fragments. The scission contour which is a hyper-surface is used to separates these two regions. The flux of the probability current passing the scission contour can be

used to evaluate the probability of observing the two fission fragments at time t . For the surface element ξ on the scission contour, the integrated flux $F(\xi, t)$ is calculated by

$$F(\xi, t) = \int_{t=0}^t dt \int_{\mathbf{q} \in \xi} \mathbf{J}(\mathbf{q}, t) \cdot d\mathbf{S}, \quad (7)$$

as in Ref. [37], in which $\mathbf{J}(\mathbf{q}, t)$ is the current

$$\mathbf{J}(\mathbf{q}, t) = \frac{\hbar}{2i} B(\mathbf{q}) [g^*(\mathbf{q}, t) \nabla g(\mathbf{q}, t) - g(\mathbf{q}, t) \nabla g^*(\mathbf{q}, t)]. \quad (8)$$

The yield of the fission product with the mass number A can be obtained by

$$Y(A) = C \sum_{\xi \in \mathcal{A}} \lim_{t \rightarrow +\infty} F(\xi, t) \quad (9)$$

where \mathcal{A} denotes an ensemble of all the surface elements ξ on the scission contour containing the fragment with mass number A , and C is the normalization factor to ensure that the total yield is normalized to be 200. In the same way, the yield of fission fragment with charge number Z can also be obtained. In this work, the computer code FELIX(version 2.0) [41] is used for describing the time evolution of the nuclear fission in TDGCM-GOA framework.

III. RESULTS AND DISCUSSION

In the adiabatic approximation approach for fission dynamic, the precise multidimensional PES is the first and the essential step toward the dynamical description of fission. Fig. 1 displayed the PES contour of ^{180}Hg obtained by the HFB calculation in the collective space of (q_{20}, q_{30}) , in which q_{20} is from -20 b to 300 b and q_{30} is from 0 b $^{3/2}$ to 40 b $^{3/2}$ with the step of $\Delta q_{20} = 2$ b and $\Delta q_{30} = 2$ b $^{3/2}$. Overall, the pattern of PES obtained in this work based on the DFT solvers HFBTHO with Skyrme SkM* functional is similar to that obtained using the symmetry unrestricted DFT solver H-FODD [6] with the same functional and that obtained using covariant density functional theory with the relativistic PC-PK1 functional [8]. The static fission path starts from a nearly spherical ground state ($q_{20} = 20$ b, $q_{30} = 0$ b $^{3/2}$), the reflection symmetric fission path can be found for small quadrupole deformations, and the reflection-asymmetric path branches away from the symmetric path about $q_{20} = 100$ b. One can see that unlike the PES of actinide nuclei, there is no valley towards to scission for ^{180}Hg , it undergoes a continuous uphill process till the mass asymmetric scission point with high q_{30} asymmetry.

In the (q_{20}, q_{30}) -constrained PES calculations by DFT, the other degree of deformations are obtained based on the variational principle. In Refs. [35, 36], it has been learned that at given q_{20} and q_{30} , there are two minimum with different value of q_{40} , and the minimum with larger q_{40} disappears when the q_{20} is large enough, which indicates the transition toward the scission. The hexadecapole deformation is an important degree of freedom for the description of PES at large

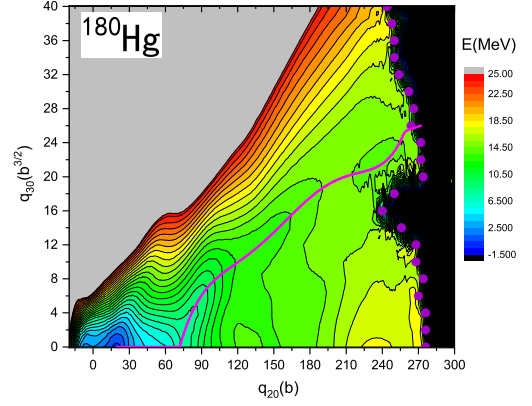


Fig. 1. (color online) Potential energy surface of ^{180}Hg in the collective space of (q_{20}, q_{30}) . The pink solid line and purple circle dots denote the static fission path and scission line respectively.

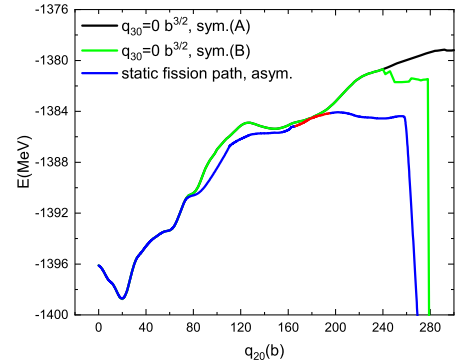


Fig. 2. (color online) HFB energies along the symmetric-fission and asymmetric-fission pathways of ^{180}Hg as a function of q_{20} . The least-energy fission pathway (static fission path) is given as a blue curve. The symmetric-fission pathways are shown as the black or green curves, labeled as (A) or (B) respectively. These two curves are obtained with different treatment of q_{40} (see text for details). The red line shows the transitional valley that bridges the asymmetric and symmetric paths.

deformation, and especially, a disturbance of hexadecapole deformation is required for a smooth and reasonable PES, as shown in Ref. [36]. Thus, in our work, at large quadrupole moments, i.e., larger than $q_{20} \simeq 200$ b ($\beta_2 \simeq 3.2$), a further constraint of hexadecapole moment q_{40} is introduced. It is done in a “perturbative” way. A smaller hexadecapole moment than the one obtained variationally is used as a further constraint in the first ten steps of DFT iterations, and it is then released to vary freely. Thus a lower energy minimum with smaller q_{40} might be obtained. This treatment is used for the calculation of PES in Fig. 1, and labeled “(B)” in Figs. 2-3. The calculation with the constraints of q_{20} and q_{30} only is labeled “(A)” in Figs. 2-3.

In Fig. 2, the energies of the static fission path as a function of quadrupole moment q_{20} are shown. The symmetric ($q_{30} = 0$ b $^{3/2}$) and the asymmetric fission path in ^{180}Hg are given respectively. One can see clearly that these energies increase with q_{20} steadily. At around $q_{20} \sim 100$ b, the asymmetric fission path starts to be favoured in energy compared to the

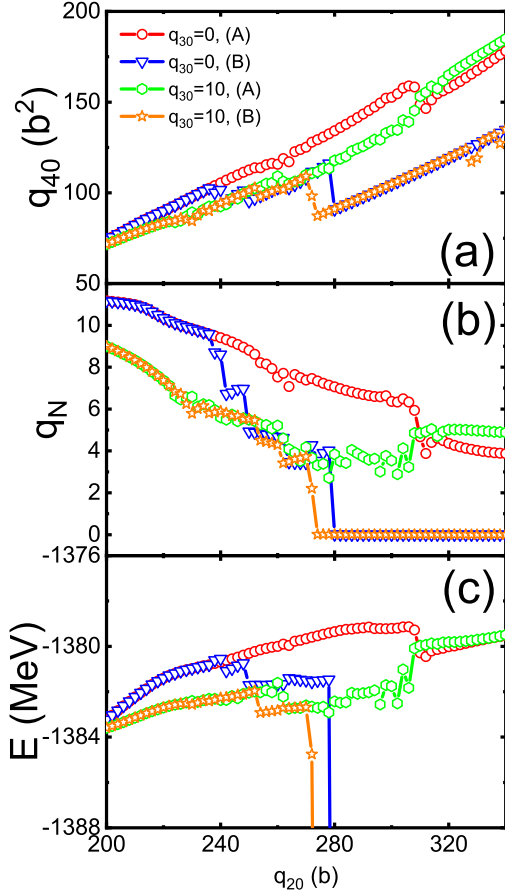


Fig. 3. (color online) The hexadecapole moment (q_{40}), the particle number of neck (q_N), and HFB energies as a function of q_{20} are shown in panels (a), (b) and (c), respectively, for $q_{30} = 0 \text{ b}^{3/2}$ and $10 \text{ b}^{3/2}$.

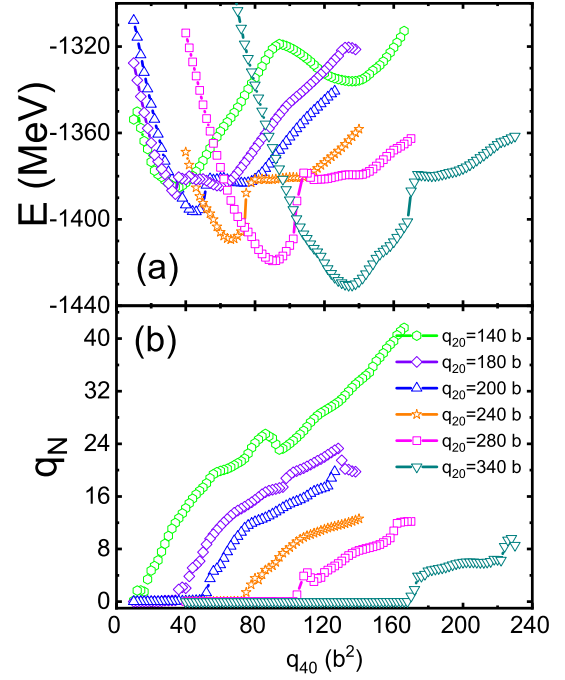


Fig. 4. (color online) HFB energies [panel (a)] and q_N [panel (b)] of ^{180}Hg obtained by the constrained q_{20} , q_{30} and q_{40} calculation. These values are shown as a function of q_{40} , and different curves are for different q_{20} values. $q_{30} = 0 \text{ b}^{3/2}$.

symmetric fission path. The transitional valley that bridges the asymmetric and symmetric paths is also drawn in red in Fig. 2. Notably, this connection occurs at the deformation where the symmetric and asymmetric paths are nearly equivalent in energy. This characteristic of ^{180}Hg also has been verified in Ref. [48] using the HFB-Gogny D1S interaction. From Fig. 2, for case (A), one can see that the energy of ^{180}Hg increase continuously with q_{20} , and it is difficult to rupture even at very large elongation, e.g. $q_{20} \geq 300 \text{ b}$ ($\beta_2 \geq 4.8$). As seen in case (B), with the inclusion of the q_{40} constraint, a gentle decent trend of the energy happens at $q_{20} \sim 240 \text{ b}$, and a sudden drop in energy occurs at $q_{20} \sim 280 \text{ b}$, indicating the nuclear scission.

In Fig. 3, the hexadecapole moment (q_{40}), the averaging particle number around the neck (q_N) and the HFB energies, are given as functions of q_{20} respectively, at given q_{30} . In order to investigate the role of q_{40} , only the region with large q_{20} is shown. From Fig. 3(a), one can see that the q_{40} increases nearly linearly till very large q_{20} value, especially for the case (A), in which the q_{40} can become very large during the elongation. After a “perturbative” constraint on q_{40} , as the case (B) in the figure, the q_{40} value has sudden drop and

then grow linearly. In the study of nuclear fission, q_N is often adopted as the indicator of the nuclear scission. For examples, $q_N = 4$ has been used for the determination of scission line of ^{240}Pu in Refs [26, 34, 49]. In Fig. 3(b), q_N decrease gradually against q_{20} . However, for case (A), the reduction of q_N become rather slow with the increase of q_{20} . Especially, at $q_{20} \sim 340 \text{ b}$ ($\beta_2 \sim 5.4$), $q_N > 4$ for $q_{30} = 0$ and $10 \text{ b}^{3/2}$, and the total energies increases continuously at large q_{20} , as seen in Fig. 3(c). After the considering of q_{40} constraint, as the case (B) shown in Fig. 3(b) and (c), both q_N and the total energy have a sudden drop at around $q_{20} \sim 280 \text{ b}$ ($\beta_2 \sim 4.5$), indicating the nuclear rupture. It is seen that when $q_N \leq 4$, q_N becomes close to zero with the increase of q_{20} .

To investigate the role of q_{40} on PES, the HFB energies and q_N against q_{40} at given q_{20} and q_{30} are plotted in Fig. 4, which are obtained through the exact constrained calculations of q_{20} , q_{30} and q_{40} . In the figure, q_{30} is constrained to be $0 \text{ b}^{3/2}$. The other q_{30} is also tested, and the results are similar as in Fig. 4. In Fig. 4(a), one can see that there are two local minima along q_{40} degree of freedom, which corresponds to distinct valleys on the multi-dimensional potential energy surface. In Ref. [36], a similar trend in ^{240}Pu has been found, and the minima related to the larger q_{40} disappears with increasing the quadruple deformation (at roughly $\beta_2 \sim 3.8$), leading to a natural transition to the minimum with the smaller q_{40} . This transition is the cause of the discontinuity and the sudden drop of energy in the two-dimensional PES of (q_{20}, q_{30}) . However, for ^{180}Hg , there remains an extremely soft and relatively flat minimum with larger q_{40} value even at very large q_{20} values, e.g. at $q_{20} = 340 \text{ b}$ ($\beta_2 \sim 5.4$). In PES calculation with only

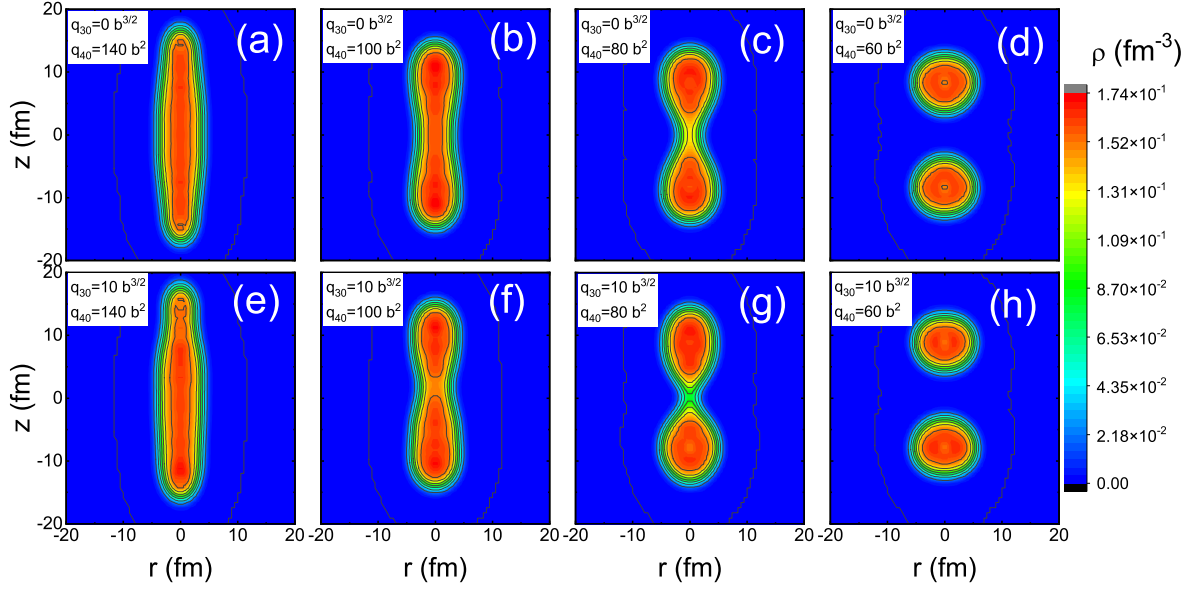


Fig. 5. (color online) Density distributions of ^{180}Hg obtained with (q_{20}, q_{30}, q_{40}) constrained calculations. Results are obtained with different constrained q_{40} for symmetric fission channel $(q_{20}, q_{30}) = (240 \text{ b}, 0 \text{ b}^{3/2})$ (upper panels) and for asymmetric fission channel $(q_{20}, q_{30}) = (240 \text{ b}, 10 \text{ b}^{3/2})$ (lower panels).

the (q_{20}, q_{30}) constraint, q_{40} degree of freedom is obtained by variations of the total energies. As seen for case (A) in Fig. 3, q_{40} after the variation calculation grows steadily even at very large q_{20} , and no transition to the minimum with smaller q_{40} happens. With only (q_{20}, q_{30}) constraint, it is difficult to find the proper scission configuration, at least for ^{180}Hg . After the “perturbative” inclusion of q_{40} constraint, as for case (B) in Fig. 3, such transition can occur at large q_{20} . In Fig. 4 (b), it is seen that q_N increase with q_{40} in general. q_N around the minimum with larger q_{40} is roughly larger than 4, and when $q_{20} > 200 \text{ b}$ its value around the minimum with smaller q_{40} is close to zero (numerically 10^{-3} - 10^{-4} , effectively near zero). For $q_N \sim 0$, the nucleus become well separated into two fragments. From this calculation, one can learn that the introduction of q_{40} constraint in the self-consistent calculation of PES can ensure the continuity of the potential energy surface. q_{40} is essential in the DFT calculation for fission study, especially for the transition to scission.

Several results of (q_{20}, q_{30}, q_{40}) constrained calculations have been shown in Fig. 5 for the density distribution profiles of ^{180}Hg . q_{20} is constrained to be 240 b , and q_{40} changes from 140 b^2 to 60 b^2 for $q_{30} = 0 \text{ b}^{3/2}$ and $q_{30} = 10 \text{ b}^{3/2}$ in the upper panel and lower panel respectively. q_{40} degree of freedom influences the formation of the neck and the scission configurations. From the figure, one can see that with large q_{40} , there is no neck in the nucleus and the nucleus is just stretched very long. For the calculation with only (q_{20}, q_{30}) constraint as the case (A) in Figs. 2-3, q_{40} has a very large value with the increase of q_{20} and thus the nucleus can not scission. With the decrease of q_{40} , the neck structure of the nucleus appears and becomes well separated when q_{40} has small values.

One of the most important quantities in induced fission is the total kinetic energy (TKE) carried out by the fission frag-

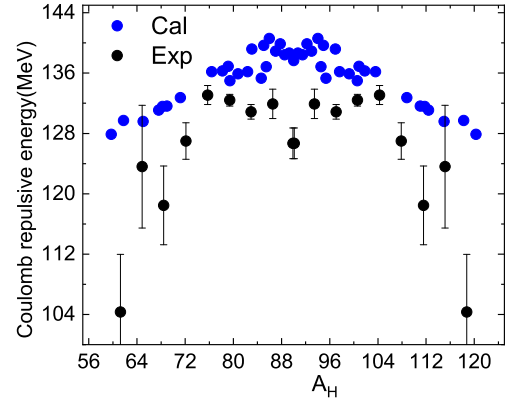


Fig. 6. (Color online) The calculated Coulomb repulsive energy of the nascent fission fragments for ^{180}Hg as functions of fragment mass, in comparison to the experimental data of the total kinetic energy [2].

ments. In this work, the total kinetic energy of the two separated fragments at scission point can be approximately estimated as the Coulomb repulsive interaction by using a simple formula $e^2 Z_H Z_L / d_{\text{ch}}$, where e stands for the proton charge, Z_H and Z_L denote the charge number of the heavy and light fragments respectively, and d_{ch} is the distance between the centers of charge of the two fragments at the scission point. Fig. 6 displays the distribution of calculated Coulomb repulsive energy based on the scission line shown by the purple circle in Fig. 1 and compared with the measured TKE [2]. It can be seen that the calculated results reproduces the trend of the measured TKE quite well, especially a dip at $A_H = 90$ and peak at $A_H = 94$, although the calculated results are generally overestimated about several MeV compared to data, which might be caused by the neglect of the dissipation effect.

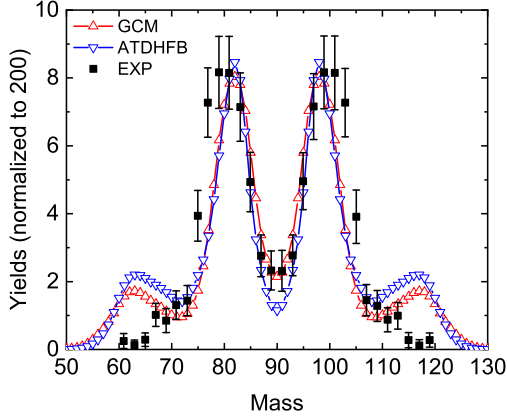


Fig. 7. (color online) Mass distribution of the fission fragments of ^{180}Hg calculated by TDGCM method (open symbols), in comparison with the experimental data (black squares) [1, 2]. The open upper triangle and lower triangle stand for the calculated results with ATDHFB mass tensor and GCM mass tensor, respectively.

Finally, we performed the TDGCM+GOA calculation to model the time evolution of the fission dynamic of ^{180}Hg . Fig. 7 shows the calculated mass distributions of the fission fragments of ^{180}Hg and compared with the experimental data [1, 2]. As one of the most important microscopic input of fission dynamic calculations, the mass tensor is calculated by GCM or ATDHFB methods in present work. The calculated mass distribution is generally similar for using the mass tensor by these two methods, and better agreement is obtained by using the GCM method for the height of asymmetric peaks and symmetric valley. Overall, the calculation reproduces the experimental data well. The calculated peak position deviates one unit from the experimental peak position. Moreover,

a more asymmetric fission mode with $A_H \sim 117$ is predicted in our calculation, which was also predicted by the covariant density functional theory with PC-PK1 functional [8].

IV. SUMMARY

In this work, the static fission properties and the fission dynamics of ^{180}Hg were investigated by the Skyrme DFT and TDGCM respectively. During the calculation of multi-dimensional PES, it is found that the hexadecapole moment is crucial to obtain a smooth PES and proper scission configurations, and thus it is essential for fission dynamic studies. For the calculation of PES with only the q_{20} and q_{30} constraints, the nuclear rupture does not happen even at very large q_{20} . Through the calculations with q_{20} , q_{30} and q_{40} constraints, it is found that a rather soft and flat minimum with large hexadecapole moment still exists in the PES of ^{180}Hg even with a very elongated shape, which hinders the transition to the lower energy minimum with smaller q_{40} . With the strategy of “perturbative” constraint of the collective freedom q_{40} , the transition to the minimum corresponding to the nuclear rupture could happen naturally, and thus reasonable scission configurations can be obtained. From these scission configurations, the estimated distribution of TKE reproduces the trend of experimental data.

Based on the static PES calculation, it is learned that asymmetric fission channel is favoured in ^{180}Hg . Finally, the fission fragment yields was calculated with the TDGCM. The calculated mass distributions also support the asymmetric fission for ^{180}Hg . The calculation agrees well with the experimental data. Moreover, a more asymmetric peak with $A_H \sim 117$ is predicted, which is also predicted by the covariant DFT with PC-PK1 parameter set [8].

- [1] A. N. Andreyev, J. Elseviers, M. Huyse, et al., New Type of Asymmetric Fission in Proton-Rich Nuclei. *Phys. Rev. Lett.* **105**, 252502 (2010). <https://doi.org/10.1103/PhysRevLett.105.252502>
- [2] J. Elseviers, A. N. Andreyev, M. Huyse, et al., β -delayed fission of ^{180}Tl , *Phys. Rev. C* **88**, 044321 (2013); 102, 019908(E) (2020). <https://doi.org/10.1103/PhysRevC.88.044321>
- [3] T. Ichikawa, A. Iwamoto, P. Möller, et al., Contrasting fission potential-energy structure of actinides and mercury isotopes. *Phys. Rev. C* **86**, 024610 (2012). <https://doi.org/10.1103/PhysRevC.86.024610>
- [4] A. V. Andreev, G. G. Adamian, N. V. Antonenko, Mass distributions for induced fission of different Hg isotopes. *Phys. Rev. C* **86**, 044315 (2012). <https://doi.org/10.1103/PhysRevC.86.044315>
- [5] P. Möller, J. Randrup, A. J. Sierk, Calculated fission yields of neutron-deficient mercury isotopes. *Phys. Rev. C* **85**, 024306 (2012). <https://doi.org/10.1103/PhysRevC.85.024306>
- [6] M. Warda, A. Staszczak, W. Nazarewicz, Fission modes of mercury isotopes. *Phys. Rev. C* **86**, 024601 (2012). <https://doi.org/10.1103/PhysRevC.86.024601>
- [7] J. D. McDonnell, W. Nazarewicz, J. A. Sheikh, et al., Excitation-energy dependence of fission in the mercury region. *Phys. Rev. C* **90**, 021302(R) (2014). <https://doi.org/10.1103/PhysRevC.90.021302>
- [8] Zeyu Li, Shengyuan Chen, Yongjing Chen, et al., Microscopic study on asymmetric fission dynamics of ^{180}Hg within covariant density functional theory. *Phys. Rev. C* **106**, 024307 (2022). <https://doi.org/10.1103/PhysRevC.106.024307>
- [9] P. Möller, J. Randrup, Calculated fission-fragment yield systematics in the region $74 \leq Z \leq 94$ and $90 \leq N \leq 150$. *Phys. Rev. C* **91**, 044316 (2015). <https://doi.org/10.1103/PhysRevC.91.044316>
- [10] V. L. Litnevsky, G. I. Kosenko, F. A. Ivanyuk, et al., Description of the two-humped mass distribution of fission fragments of mercury isotopes on the basis of the multidimensional stochastic model. *Phys. At. Nucl.* **77**, 167 (2014). <https://doi.org/10.1103/PhysRevC.91.044316>
- [11] A. V. Andreev, G. G. Adamian, N. V. Antonenko, et al., Isospin dependence of mass-distribution shape of fission fragments of Hg isotopes. *Phys. Rev. C* **88**, 047604 (2013). <https://doi.org/10.1103/PhysRevC.88.047604>
- [12] S. Panebianco, J.-L. Sida, H. Goutte, et al., Role of deformed shell effects on the mass asymmetry in nuclear fis-

- sion of mercury isotopes. Phys. Rev. C **86**, 064601 (2012). <https://doi.org/10.1103/PhysRevC.86.064601>
- [13] M. Warda and A. Zdeb, Fission fragment mass yield deduced from density distribution in the pre-scission configuration. Phys. Scr. **90**, 114003 (2015). <https://doi.org/10.1088/0031-8949/90/11/114003>
- [14] L. Meitner, O.R. Frisch, Disintegration of Uranium by Neutrons: a New Type of Nuclear Reaction. Nature (London) **143**, 239 (1939). <https://doi.org/10.1038/143239a0>
- [15] N. Bohr, J.A. Wheeler, The Mechanism of Nuclear Fission. Phys. Rev. **56**, 426 (1939). <https://doi.org/10.1103/PhysRev.56.426>
- [16] P. Möller, D.G. Madland, A.J. Sierk, Nuclear fission modes and fragment mass asymmetries in a five-dimensional deformation space. Nature (London) **409**, 785 (2001). <https://doi.org/10.1038/35057204>
- [17] Yu.V. Pyatkov, V.V. Pashkevich, A.V. Unzhakova, et al., Manifestation of clustering in the $^{252}\text{Cf}(\text{fs})$ and $^{249}\text{Cf}(\text{n,h,f})$ reactions. Nuclear Phys. A **624**, 140 (1997). [https://doi.org/10.1016/S0375-9474\(97\)00417-X](https://doi.org/10.1016/S0375-9474(97)00417-X)
- [18] K. Pomorski, B. Nerlo-Pomorska, J. Bartel, et al., Stability of superheavy nuclei. Phys. Rev. C **97**, 034319 (2018). <https://doi.org/10.1103/PhysRevC.97.034319>
- [19] K. Pomorski, A. Dobrowolski, R. Han, et al., Mass yields of fission fragments of Pt to Ra isotopes. Phys. Rev. C **101**, 064602 (2020). <https://doi.org/10.1103/PhysRevC.101.064602>
- [20] M. Warda, J.L. Egido, L.M. Robledo, et al., Self-consistent calculations of fission barriers in the Fm region. Phys. Rev. C **66**, 014310 (2002). <https://doi.org/10.1103/PhysRevC.66.014310>
- [21] T.R. Rodriguez, J.L. Egido, Triaxial angular momentum projection and configuration mixing calculations with the Gogny force. Phys. Rev. C **81**, 064323 (2010). <https://doi.org/10.1103/PhysRevC.81.064323>
- [22] N. Hinohara, T. Nakatsukasa, M. Matsuo, et al., Microscopic description of oblate-prolate shape mixing in proton-rich Se isotopes. Phys. Rev. C **80**, 014305 (2009). <https://doi.org/10.1103/PhysRevC.80.014305>
- [23] L. Bonneau, Fission modes of ^{256}Fm and ^{258}Fm in a microscopic approach. Phys. Rev. C **74**, 014301 (2006). <https://doi.org/10.1103/PhysRevC.74.014301>
- [24] Y. J. Chen, Y. Su, G. X. Dong et al., Energy density functional analysis of the fission properties of ^{240}Pu : The effect of pairing correlations. Chin. Phys. C **46**, 024103 (2022). <https://doi.org/10.1088/1674-1137/ac347a>
- [25] Y. J. Chen, Y. Su, L. L. Liu et al., Microscopic study of neutron-induced fission process of ^{239}Pu via zero- and finite-temperature density functional theory. Chin. Phys. C **47**, 054103 (2023). <https://doi.org/10.1088/1674-1137/acbe2c>
- [26] Yang Su, Ze-Yu Li, Li-Le Liu, et al., Sensitivity impacts owing to the variations in the type of zero range pairing forces on the fission properties using the density functional theory, Nucl. Sci. Tech. **35**, 62 (2024). <https://doi.org/10.1007/s41365-024-01422-4>
- [27] J.-Y. Guo, P. Jiao, X.-Z. Fang, Microscopic description of nuclear shape evolution from spherical to octupole-deformed shapes in relativistic mean-field theory. Phys. Rev. C **82**, 047301 (2010). <https://doi.org/10.1103/PhysRevC.82.047301>
- [28] H. Tao, J. Zhao, Z. P. Li et al., Microscopic study of induced fission dynamics of ^{226}Th with covariant energy density functionals. Phys. Rev. C **96**, 024319 (2017). <https://doi.org/10.1103/PhysRevC.96.024319>
- [29] M. H. Zhou, Z. Y. Li, S. Y. Chen et al., Three-dimensional potential energy surface for fission of ^{236}U within covariant density functional theory. Chin. Phys. C **47**, 064106 (2023). <https://doi.org/10.1088/1674-1137/acc4ac>
- [30] J. Zhao, T. Nikšić, and D. Vretenar, Microscopic self-consistent description of induced fission: Dynamical pairing degree of freedom. Phys. Rev. C **104**, 044612 (2021). <https://doi.org/10.1103/PhysRevC.104.044612>
- [31] A. Zdeb, M. Warda, L.M. Robledo, Description of the multidimensional potential-energy surface in fission of ^{252}Cf and ^{258}No . Phys. Rev. C **104**, 014610 (2021). <https://doi.org/10.1103/PhysRevC.104.014610>
- [32] N. Dubray and D. Regnier, Numerical search of discontinuities in self-consistent potential energy surfaces. Comput. Phys. Commun. **183**, 2035 (2012). <https://doi.org/10.1016/j.cpc.2012.05.001>
- [33] D. Regnier, N. Dubray, N. Schunck, From asymmetric to symmetric fission in the fermion isotope within the time-dependent generator-coordinate-method formalism. Phys. Rev. C **99**, 024611 (2019). <https://doi.org/10.1103/PhysRevC.99.024611>
- [34] N. Schunck, D. Duke, H. Carr et al., Description of induced nuclear fission with Skyrme energy functionals: Static potential energy surfaces and fission fragment properties. Phys. Rev. C **90**, 054305 (2014). <https://doi.org/10.1103/PhysRevC.90.054305>
- [35] J.F. Berger, M. Girod, D. Gogny, Microscopic analysis of collective dynamics in low energy fission. Nucl. Phys. A **428**, 23 (1984). [https://doi.org/10.1016/0375-9474\(84\)90240-9](https://doi.org/10.1016/0375-9474(84)90240-9)
- [36] J.H. Chi, Y. Qiang, C.Y. Gao, et al., Role of hexadecapole deformation in fission potential energy surfaces of ^{240}Pu . Nucl. Phys. A **1032**, 122626 (2023). <https://doi.org/10.1016/j.nuclphysa.2023.122626>
- [37] D. Regnier, N. Dubray, N. Schunck, et al., Fission fragment charge and mass distributions in $^{239}\text{Pu}(\text{n,f})$ in the adiabatic nuclear energy density functional theory. Phys. Rev. C **93**, 054611 (2016). <https://doi.org/10.1103/PhysRevC.93.054611>
- [38] M. Bender, P. H. Heenen, P. G. Reinhard, Self-consistent mean-field models for nuclear structure. Rev. Mod. Phys. **75**, 121 (2003). <https://doi.org/10.1103/RevModPhys.75.121>
- [39] J. F. Berger, M. Girod, D. Gogny, Time-dependent quantum collective dynamics applied to nuclear fission. Comput. Phys. Commun. **63**, 365 (1991). [https://doi.org/10.1016/0010-4655\(91\)90263-K](https://doi.org/10.1016/0010-4655(91)90263-K)
- [40] R. Bernard, H. Goutte, D. Gogny, et al., Microscopic and nonadiabatic Schrödinger equation derived from the generator coordinate method based on zero- and two-quasiparticle states. Phys. Rev. C **84**, 044308 (2011). <https://doi.org/10.1103/PhysRevC.84.044308>
- [41] D. Regnier, N. Dubray, M. Verriere, et al., FELIX-2.0: New version of the finite element solver for the time dependent generator coordinate method with the Gaussian overlap approximation. Comput. Phys. Commun. **225**, 180 (2018). <https://doi.org/10.1016/j.cpc.2017.12.00>
- [42] E. Perlińska, S. G. Rohoziński, J. Dobaczewski et al., Local density approximation for proton-neutron pairing correlations: Formalism. Phys. Rev. C **69**, 014316 (2004). <https://doi.org/10.1103/PhysRevC.69.014316>
- [43] J. Dobaczewski and J. Dudek, Time-odd components in the mean-field of rotating superdeformed nuclei, Phys. Rev. C **52**, 1827 (1995). <https://doi.org/10.1103/PhysRevC.52.1827>
- [44] N. Schunck and L.M. Robledo, Microscopic theory of nuclear fission: a review. Rep. Prog. Phys. **79**, 116301 (2016). <https://doi.org/10.1088/0034-4885/79/11/116301>
- [45] R. Navarro Perez, N. Schunck, R. D. Lasserri et al.,

- 553 Axially deformed solution of the Skyrme-Hartree-Fock- 562
 554 Bogolyubov equations using the transformed harmonic os- 563
 555 cillator basis (III) hfbtho (v3.00): A new version of 564
 556 the program. *Comput. Phys. Commun.* **220**, 363 (2017). 565
 557 <https://doi.org/10.1016/j.cpc.2017.06.022> 566
- 558 [46] J. Bartel, P. Quentin, M. Brack, et al., Towards a better 567
 559 parametrisation of Skyrme-like effective forces: A critical 568
 560 study of the SkM force. *Nucl. Phys. A* **386**, 79 (1982). 569
 561 [https://doi.org/10.1016/0375-9474\(82\)90403-1](https://doi.org/10.1016/0375-9474(82)90403-1) 570
- 571 [47] M. Warda, A. Staszczak, L. Próchniak, Comparison of 572
 self-consistent Skyrme and Gogny calculations for light 573
 Hg isotopes. *Int. J. Mod. Phys. E* **19**, 787 (2010). 574
<https://doi.org/10.1142/S0218301310015230> 575
- [48] R. N. Bernard, C. Simenel, G. Blanchon, et al. Fission of 576
 ^{180}Hg and ^{264}Fm : a comparative study. *Eur. Phys. J. A* **60**, 577
 192 (2024). <https://doi.org/10.1140/epja/s10050-024-01415-2> 578
- [49] X. B. Wang, Yongjing Chen, G. X. Dong, et al., Role of pairing 579
 correlations in the fission process. *Phys. Rev. C* **108**, 034306 580
 (2023). <https://doi.org/10.1103/PhysRevC.108.034306> 581